

Spherical iron Phosphate Prepared via Liquid Precipitation-Spray Drying Method and Its Application as the Precursor of Lithium Iron Phosphate

Ju Guo^{1,2,3}, JianXin Cao^{1,*}, ShuangZhu Jia^{1,4}

¹ College of Chemistry and Chemical Engineering, Guizhou University, Guiyang 550025, Guizhou, China

² Moutai Institute, Renhuai 564507, Guizhou, China

³ State Key Laboratory for Efficient Utilization of Low-and Medium-grade Phosphate Ores and Their Associated Resources, Guiyang 550025, Guizhou, China

⁴ Qiannan Normal University for Nationalities, Duyun 558000, Guizhou, China

*E-mail: 3429958828@qq.com

Received: 3 January 2020 / Accepted: 28 February 2020 / Published: 31 August 2020

In this work, spherical iron phosphate was prepared via a simple liquid precipitation-spray drying method, which could overcome the disadvantages of hydrothermal method, such as harsh reaction conditions and the requirement of additives. The materials were characterized by means of XRD, FTIR, ICP, XPS, SEM, TEM. The results showed that as-prepared sample was amorphous $\text{FePO}_4 \cdot 2\text{H}_2\text{O}$, which possess regular spherical shape, uniform particle size, small particle size (ca. 1.9 μm) and high specific surface area. The spherical iron phosphate was then converted into lithium iron phosphate material, which could exhibit excellent energy storage capacity. The first discharge specific capacity of the resulting lithium iron phosphate material is 155.6, 149, 119.1 and 103.8 mAh/g respectively at 0.5, 1, 5 and 10 C ratio. As a consequence, the present work opens a new strategy for the preparation of high performance lithium iron phosphate electrode materials.

Keywords: spherical iron phosphate; simple preparation; lithium iron phosphate; performance

1. INTRODUCTION

Iron phosphate is an important chemical materials, which was widely used in the fields of photocatalyst [1-2], wastewater treatment [3-4], metal material rust prevention [5-7], crop fertilizer [8], etc. In recent years, iron phosphate has been increasingly used as the precursor of lithium iron phosphate, known as the cathode material of lithium battery [9-11]. Compared with other precursors,

such as ferrous oxalate, iron oxide, ferric chloride and iron nitrate [12-16], iron phosphate has the advantages of low price, environmental-friendly and high thermal stability [17-20].

Carbothermal reduction is commonly used to synthesize lithium iron phosphate, during which iron phosphate is reduced via a solid-phase reaction under high temperature and reducing atmosphere upon the addition of lithium and carbon [21-23]. The materials need to go through a series process, such as reactant diffusion, reaction, nucleation, and growth. Thus, the morphology of iron phosphate has significant influence on the properties of the resulting lithium iron phosphate. For instance, the surface area and contact area of the reactants have an strong influence on the kinetics of the solid phase reaction [24]. Compared with other morphologies, spherical sample possessing high specific surface area could provide large contact area for the solid phase reaction, and then improve the reaction and diffusion rate of the product layer, which could avoid sample sintering under high temperature solid phase reaction. This is conducive to obtaining regular spherical lithium iron phosphate, which is readily to display high electrochemical performance. Because spherical shape materials could provide short lithium ion and electron transport distance, increase the contact area between electrode material and electrolyte [22-23]. Therefore, lithium iron phosphate synthesized using spherical iron phosphate as precursor is attract more and more attention with the aim of obtaining high performance materials for lithium battery [25-29].

Hydrothermal method is commonly used for the synthesis of spherical iron phosphate, which uses soluble iron salts and phosphates as raw materials, alkaline substances as precipitants [30-32]. Hydrothermal reaction is generally involve a dissolution-crystallization equilibrium process, which is effective to control the morphology of crystals [25]. However, hydrothermal synthesis often need to be performed under high temperature, high pressure and even ultrasound conditions [27, 30-34]. Moreover, chemical agents or templates are often used as morphology aids to control the crystallization process [20, 26], so as to improve the consistency of the crystal particle size and/or obtain materials possessing unique microstructure. As a consequence, hydrothermal synthesis is difficult to be used in large scale, and developing simple method performed under mild synthesis conditions is very attractive.

In order to overcome the troublesome problems of hydrothermal synthesis, we develop a novel technology for the preparation of spherical iron phosphate via liquid phase precipitation-spray drying strategy. Firstly, nano-scale iron phosphate colloid is prepared via a liquid-phase precipitation method under mild reaction conditions. No additional reactant was added to control the morphology of the colloid during the synthesis procedure, which greatly simplify the filtration and washing process. However, the as-prepared iron phosphate colloid agglomerate seriously, which would lead to severe sintering during the subsequent drying process [21, 35]. For comparison, the nanoscale iron phosphate colloidal could disperse into small spherical droplets with uniform particle size after spray drying. And thus, secondary particles of iron phosphate with good spherical consistency and uniform particle size could be obtained. We find that the average size of the sphere is about 1.9 μm , which is 79.4% smaller than that of the samples prepared by hydrothermal method. Taking the advantages of liquid phase precipitation and spray drying, we successfully obtain well-shaped and homogenously dispersed spherical iron phosphate, and thus the resulting lithium iron phosphate material could exhibit excellent electrochemical performance.

Herein, in this work, iron sulfate, phosphoric acid and ammonia were used as the raw materials to prepare spherical ferric phosphate by liquid phase precipitation-spray drying and hydrothermal method, respectively. The differences of the structure, morphology, particle size and specific surface area of iron phosphate obtained by different methods were compared. Lithium iron phosphate / carbon composites were synthesized from spherical iron phosphate obtained by different methods under the same conditions, and their electrochemical properties were compared.

2. EXPERIMENTAL

2.1 Raw materials and equipment

Raw materials: iron sulfate; phosphoric acid; ammonia water; lithium carbonate; cetyltrimethylammonium bromide (CTAB); glucose; anhydrous ethanol, etc., all of the above reagents are of analytical grade and used without further purification. Equipment: hydrothermic kettle, peristaltic pump, acidity meter, laboratory type spray dryer, electric heating air drying oven, tubular resistance furnace, etc.

2.2 Experimental methods

2.2.1 Preparation of spherical iron phosphate by liquid precipitation-spray drying method

The process flow diagram of liquid phase precipitation-spray drying method for preparing spherical iron phosphate is shown in Figure 1a. Phosphoric acid solution ($\omega=30\%$) was added to the reaction kettle in advance, then the iron sulfate solution ($\omega=4\%$) was slowly added to the reaction kettle by a peristaltic pump under stirring. The amount ratio of phosphoric acid and iron sulfate added was 1.05:1. The reaction temperature was controlled at $60\text{ }^{\circ}\text{C}$ and the pH of the reaction solution was controlled to 2.5 using an aqueous ammonia solution ($\omega=5\%$). Different samples were prepared at reaction time of 3, 6, and 10 h, respectively. After the reaction was finished, it was filtered and washed. The washed filter cake was mixed with deionized water to form a mixed solution having a solid content of 20%. Drying was carried out by means of a spray dryer, the feed flow rate was controlled to 2 ml/min, and the drying temperature was $180\text{ }^{\circ}\text{C}$ to obtain products, which was designated as FP-a (3h), FP-a (6h), and FP-a (10h).

2.2.2 Preparation of spherical iron phosphate by hydrothermal method

The process flow diagram of hydrothermal method for preparing spherical iron phosphate is shown in Figure 1b. Phosphoric acid solution ($\omega=30\%$) and CTAB solution ($\omega=0.1\%$) were added to the reaction kettle in advance, then the iron sulfate solution ($\omega=4\%$) was slowly added to the reaction kettle by a peristaltic pump under stirring. The amount ratio of phosphoric acid and iron sulfate added was 1.05:1. The temperature was controlled at $180\text{ }^{\circ}\text{C}$ during the reaction and the pH of the reaction

solution was controlled to 2.5 using an aqueous ammonia solution ($\omega=5\%$). Different samples were prepared at reaction time of 3, 6, and 10 h, respectively. After the reaction was finished, it was filtered and washed. The product was dried by an electric blast drying oven for 4 hours, and the drying temperature was 120°C to obtain products, which were respectively recorded as FP-b (3h), FP-b (6h), and FP-b (10h).

2.2.3 Preparation of LiFePO_4/C

The process flow diagram is shown in Figure 1c. Iron phosphate prepared above and lithium carbonate were weighed according to the amount ratio of 0.52:1, glucose and ethanol were added, mixed uniformly. It was pre-calcined at 350°C for 4 h in a nitrogen atmosphere, then calcined at 750°C for 8 h, cooled and ground, and then LiFePO_4/C composite material was obtained. The composite material synthesized by FP-a (10h) was recorded as LFP/C-a, and the composite material synthesized by FP-b (10h) was recorded as LFP/C-b.

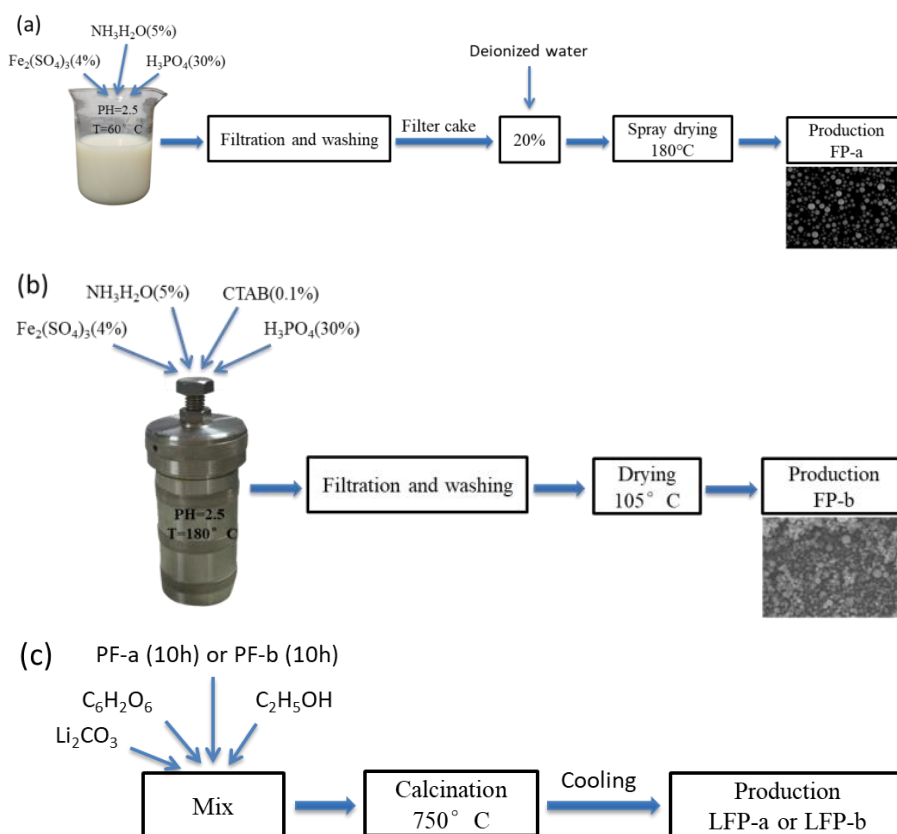


Figure 1. The process flow diagrams of samples ; (a)FP-a, (b)FP-b, (c)LFP-a/b

2.3 Characterization

The contents of Li, Fe, P and N elements in the samples were analyzed by inductively coupled plasma spectrometer (ICP) (PEOptima 7000, USA) and Kjeldahl (Shanghai Xinjia KDN-C);

Characterization of the element was performed with an X-ray photoelectron spectroscopy (XPS) and X-ray energy spectrometer (EDS); the structure of the sample was characterized by X-ray diffractometry (XRD) (X'Pert Powder III); using infrared FT-IR (American Thermo Scientific Nicolet-IS10) to characterize the functional structure of the sample, the wave number measurement range is 400-4000 cm^{-1} ; the sample water content and heat are tested by a synchronous thermal analyzer (Nexus STA449C, Germany) Stability, test range 35-800 ° C, heating rate 10 ° C / min.

The morphology and particle size of the samples were observed by a tungsten filament scanning electron microscope (SEM) (German ZEMA-500) and field transmission electron microscopy (TEM) (Tecnal G2 F20 S-TWIN, FEI, USA); the sample size was measured using a Zeta potentiometer and a laser particle size analyzer; the specific surface area of the sample was tested using a specific surface and pore size analyzer (Conta NOVA 1000E).

2.4 Battery assembly and electrochemical performance test

Battery assembly: LiFePO_4/C composite prepared above was used as active material, acetylene black was used as conductive agent, and polyvinylidene fluoride was used as binder. N-methyl-2-pyrrolidone was used as solvent. The slurry was applied to an aluminum foil, and dried at 120 ° C for 12 hours under vacuum to prepare a wafer as a positive electrode sheet. Lithium plate was used as the negative electrode, 1 mol/L LiPF_6 ethylene carbonate/dimethyl carbonate (1:1 by volume) solution was used as the electrolyte, and polypropylene microporous film was used as the separator of the battery. The battery was assembled into a CR2032 button battery in the glove box. The glove box environment was argon atmosphere, the oxygen content was less than 10ppm, the water content was less than 2.5ppm.

Electrochemical performance test: Wuhan blue electric battery test system (LAND-BT2013A) was used to test different rate constant current charge and discharge and cycle performance at room temperature. The test voltage range was 2.0-4.2V. Cyclic volt-ampere curve (CV) and AC impedance (EIS) were tested using Shanghai Chenhua CHI760D electrochemical workstation. The CV test conditions were voltage range 2.3-4.2V, frequency was 0.1mV/s, and EIS test conditions were frequency 100kHz-10mHz, the excitation voltage is 5 mv.

3. RESULTS AND DISCUSSION

3.1 Composition and structure

Figure 2a are the XRD spectrums of FP-a samples prepared by liquid phase precipitation-spray drying at different reaction times (3, 6 and 10 h), the attached table shows the Fe, P, and N element contents. It can be seen from Fig. 2a that no characteristic diffraction peaks are observed of all the samples, showing a typical amorphous structure [8, 36]. The results in the attached table show that the Fe and P contents are stable, all of them meet the Chinese standard for battery grade iron phosphate industry (HG/T4701-2014). However, a trace amount of N element is detected in the samples also,

and it increases slightly with the extension of the reaction time, which is caused by the encapsulation of the impurity N ion during the preparation of the FP-a samples [1]. Figure 2b shows the XRD spectrums of the FP-b samples prepared by hydrothermal method at different reaction times (3, 6, 10h), the attached table shows the content of Fe, P and N element contents. It can be seen from Fig. 2b that all the XRD spectrums of FP-b samples show significant diffraction peaks, indicating that the samples have good crystallinity. It is found that the FP-b samples are consistent with the material diffraction peaks of the JCPDS cards (01-082-1164), and its molecular formula is $\text{Fe}_2(\text{NH}_4)\text{OH}(\text{PO}_4)_2(\text{H}_2\text{O})_2$, belonging to the monoclinic system, and the space group is $\text{P}2_1/\text{C}$. The attached table shows that the Fe and P contents of the FP-b samples are slightly higher than the FP-a samples, while the N content is significantly higher than that of FP-a samples. This is consistent with the theoretical value of the N content in the molecular formula obtained from the XRD spectrum of the FP-b sample, indicating that N in the FP-b sample forms a complex with iron phosphate. Figure 2c and Figure 2d show the EDS spectrums of FP-a (10h) and FP-b (10h) samples, respectively. The results show that the FP-a sample contains Fe, P, O elements, and no N is detected, while the FP-b sample contains Fe, P, O, and N elements. The C element is also detected in the two samples, which was due to the pretreatment of the samples by carbon injection. The EDS spectrums results further confirm the XRD spectrum results.

It can be seen from the above results that the iron phosphate samples prepared by the liquid phase precipitation-spray drying method and the hydrothermal method have significant structural differences. The FP-a sample is amorphous iron phosphate, while the FP-b sample is a crystalline iron ammonium phosphate complex. This is consistent with the findings of Liu [48], Song [37]. Liu's research results show that the main reaction equations in the preparation of iron phosphate by liquid precipitation method are:

- (1) $\text{Fe}^{3+} + \text{H}_2\text{O} = \text{Fe}(\text{OH})^{2+} + \text{H}^+$;
- (2) $\text{Fe}(\text{OH})^{2+} + \text{H}_2\text{O} = \text{Fe}(\text{OH})^+ + \text{H}^+$;
- (3) $\text{Fe}^{3+} + \text{H}_3\text{PO}_4 = \text{FeH}_2\text{PO}_4^{2+} + \text{H}^+$;
- (4) $\text{FeH}_2\text{PO}_4^{2+} + \text{H}_3\text{PO}_4 = \text{Fe}(\text{H}_2\text{PO}_4)_2^+ + \text{H}^+$;
- (5) $\text{Fe}(\text{OH})^+ + \text{Fe}(\text{H}_2\text{PO}_4)_2^+ = 2\text{FePO}_4 \cdot 2\text{H}_2\text{O} + 2\text{H}^+$,

Therefore, the product obtained by the liquid phase precipitation method is iron phosphate dihydrate, which has a certain probability of encapsulating a trace amount of N; Song's research shows that the main reaction equations in the preparation of iron phosphate by hydrothermal method are: (1) $\text{HPO}_4^{2-} + \text{H}_2\text{O} = \text{H}_2\text{PO}_4^- + \text{OH}^-$; (2) $\text{HPO}_4^{2-} = \text{H}^+ + \text{PO}_4^{3-}$; (3) $\text{Fe}^{3+} + 3 \text{OH}^- = \text{Fe}(\text{OH})_3 \downarrow$; (4) $\text{Fe}^{3+} + \text{PO}_4^{3-} = \text{FePO}_4 \downarrow$; (5) $5 \text{Fe}^{3+} + 4 \text{HPO}_4^{2-} + 5\text{H}_2\text{O} = \text{Fe}(\text{PO}_4)_4(\text{OH})_3 \cdot 2\text{H}_2\text{O} \downarrow + 7 \text{H}^+$, and with different hydrothermal conditions, the formed iron phosphate and ammonia water further reaction to form different ammonium iron phosphate complexes, resulting in higher N content in the product. Therefore, the difference in the reaction mechanism between the liquid phase precipitation-spray drying method and the hydrothermal method for preparing iron phosphate results in a difference in the structure and composition of the FP-a and FP-b samples.

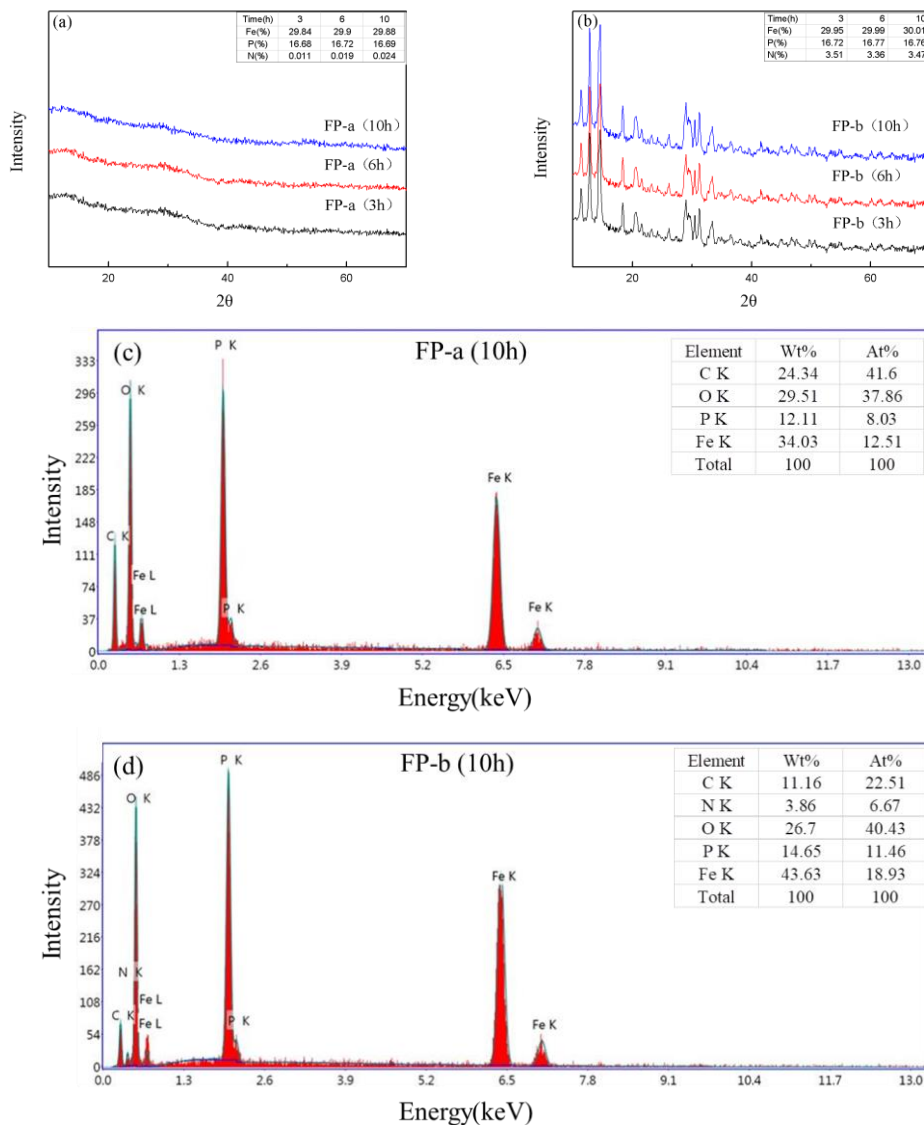


Figure 2. XRD (a, b), EDS (c, d) spectrums of FP-a and FP-b samples (The attached table is the sample element content)

In order to further analyze the structural differences between FP-a and FP-b samples, TG-DSC and FT-IR analysis are performed on them, and the results are shown in Figures 3a and 3b. The TG curves in Figure 3a show that the total weight loss rate of the FP-a (10h) sample is 19.47%, which is basically consistent with the theoretical weight loss rate of the two crystal waters removed by the formula $\text{FePO}_4 \cdot 2\text{H}_2\text{O}$. The total weight loss rate of the FP-b (10h) sample is 19.86%, which is basically consistent with the theoretical weight loss rate of the molecular formula $\text{Fe}_2(\text{NH}_4)\text{OH}(\text{PO}_4)_2(\text{H}_2\text{O})_2$ after decrystallization and ammonia decomposition. The TG curve test results confirm the speculation of the structure of the samples by the XRD spectrums, which can also be proved from the DSC curve test results. From the DSC curve test results in Figure 3a, we can see that the FP-a (10h) sample has a significant endothermic peak at 187.01 °C, corresponding to the absorption heat of two crystal waters [1, 37], The reaction equation is: $\text{FePO}_4 \cdot 2\text{H}_2\text{O} = \text{FePO}_4 + 2\text{H}_2\text{O}\uparrow$;

FP-b (10h) samples have significant endothermic peaks at 140.43, 288.59 and 537.13 °C, corresponding to the heat of absorption of crystal water removal, decomposition and phase structure transition [38-39], The reaction equations are : (1) $Fe_2(NH_4)OH(PO_4)_2 \cdot (H_2O)_2 = Fe_2(NH_4)OH(PO_4)_2 + 2H_2O \uparrow$; (2) $Fe_2(NH_4)OH(PO_4)_2 = 2FePO_4 + NH_3 \uparrow + H_2O \uparrow$. Figure 3b is an FT-IR spectrums of FP-a (10h) and FP-b (10h) samples at a wavenumber of 400-4000 cm^{-1} . It can be seen that the FP-a (10h) and FP-b (10h) samples have the same vibration peak at the wave numbers of 526.13, 1047.63, and 1428.66 cm^{-1} , which belong to the symmetric stretching vibration peak of the P-O bond. The FP-b (10h) sample has an asymmetric stretching vibration peak of P-O bond at wave number 984.13 cm^{-1} [17, 40]; FP-a (10h) and FP-b (10h) samples have vibration peaks attributed to O-H at wave numbers of 1645.87 and 3225.87 cm^{-1} [38]; The FP-b (10h) sample has a vibrational peak attributed to N-H at a wavenumber of 3188.04 cm^{-1} [41], while the FP-a (10h) sample does not. This is due to the presence of NH_4^+ in the FP-b (10h) sample and also demonstrates the accuracy of the FP-b (10h) spectrum results.

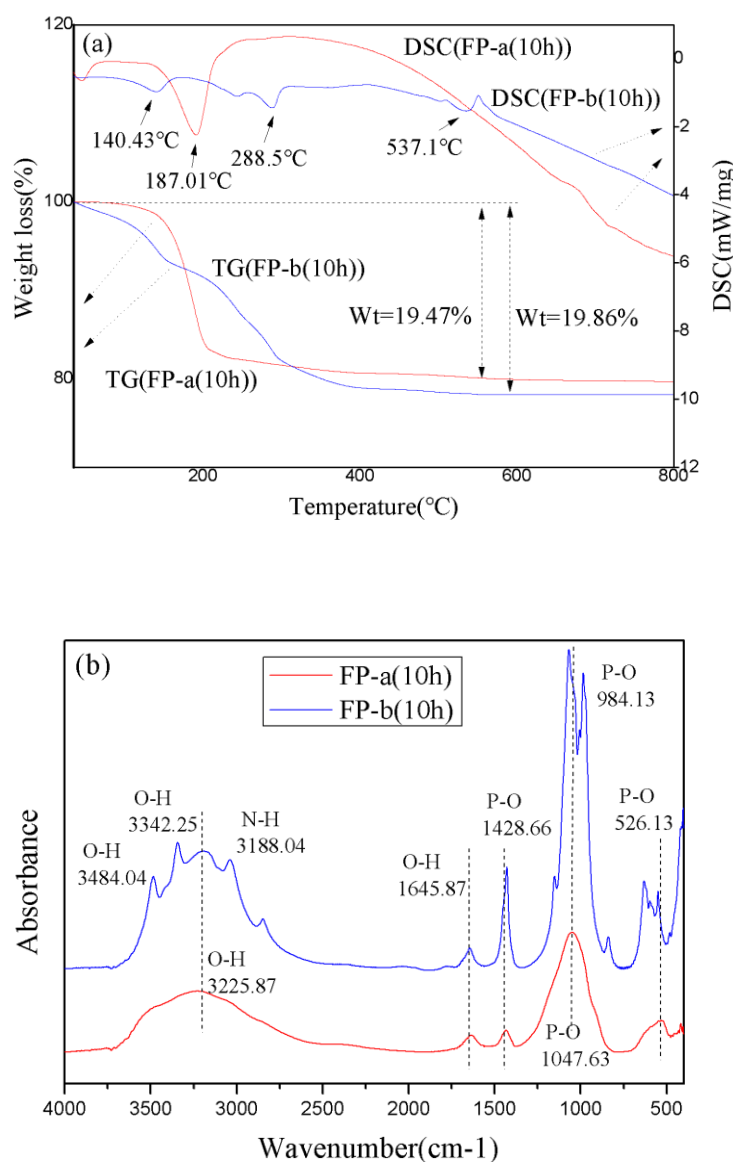
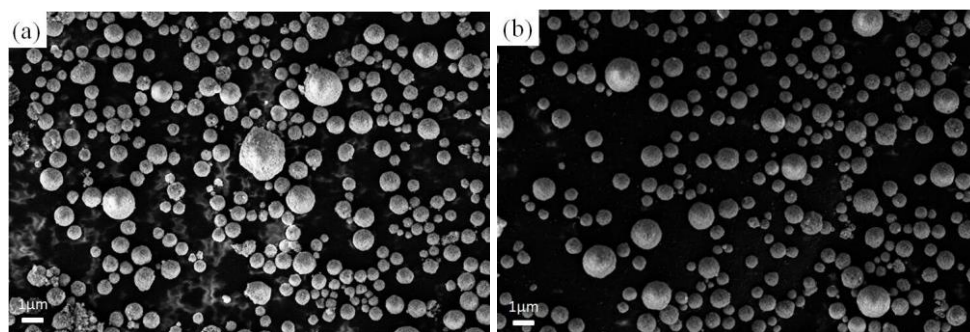


Figure 3. TG-DSC (a) and FT-IR (b) spectrums of FP-a (10h) and FP-b (10h) samples

3.2 Morphology and Size

In order to study the morphology and particle size differences of FP-a and FP-b samples, the samples are analyzed by SEM, Zeta potential meter and laser particle size analyzer. The results are shown in Figures 4 and 5. Figures 4a, b, and c are SEM images of FP-a samples at 3, 6, and 10 h, respectively, the results show that the FP-a samples prepared at different reaction times exhibit a regular spherical particle morphology with small size, and the particle size distribution is uniform. Figures 4d, e, and f are SEM images of FP-b samples at 3, 6, and 10 h respectively, the results show that the sphericity of the samples increases gradually with the extension of the reaction time, while the dispersion is poor and there is a slight agglomeration, the particle size is also larger than that of the FP-a samples, and the particle size of the FP-b samples tend to increase slightly as the reaction time increases. The reason for this difference is due to that a large number of fine primary iron phosphate particles are formed in the process of preparing iron phosphate by liquid phase precipitation-spray drying method, and the iron phosphate solution is dispersed into fine by a spray-drying nozzle, the spherical iron phosphate droplets formed after the water was dried, so the sphericity is high and the particle size distribution is uniform [35]. However, in the process of preparation of iron phosphate product by hydrothermal method, the particles gradually increase and form spherical particle morphology under the action of high temperature and CTAB [26].

Figure 5a is particle size distribution of the FP-a samples at 3, 6, and 10 h, respectively. The results show that the particle size distribution of the samples is uniform at different reaction times, and the particle size remains basically the same as the reaction time increases, the average particle diameters of the FP-a (3h), FP-a (6h), and FP-a (10h) samples are 1.908, 1.912, and 1.919 μm , respectively. Fig. 5b is particle size distribution of FP-b samples at 3, 6, and 10 h respectively. The results show that the particle size distribution of the samples in different reaction time are wide, showing "shoulders", and with the reaction time increasing, the particle size increase slightly, the average particle sizes of FP-b (3h), FP-b (6h) and FP-b (10h) samples are about 3.196, 5.97 and 9.318 μm , respectively, the particle size is larger than FP-a, and the particle size distribution is wider than the FP-a samples also. This is consistent with the sample SEM images obtained in Figure 4.



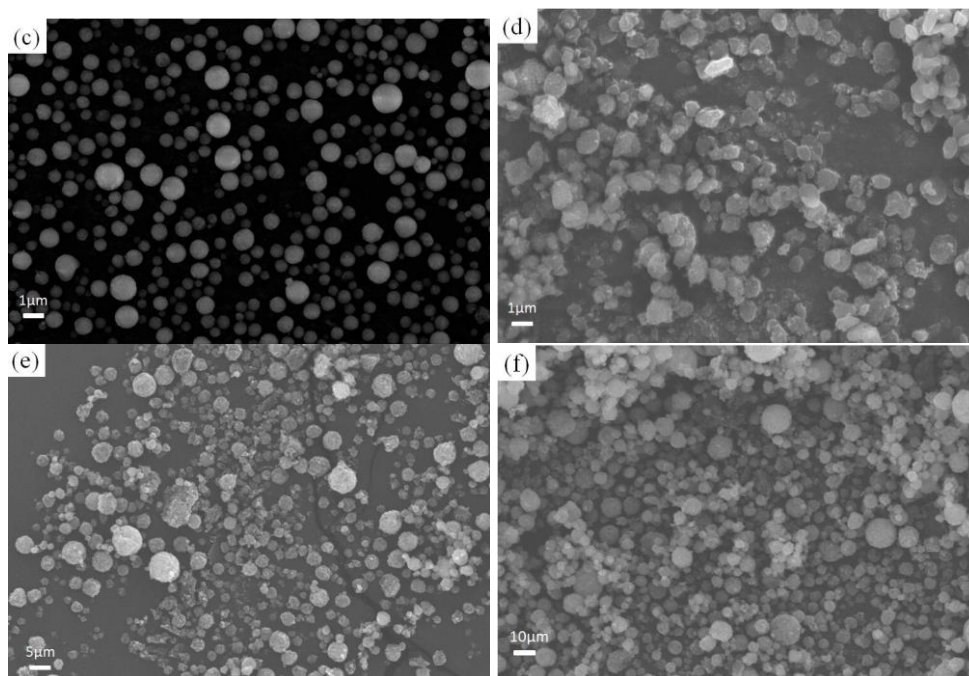


Figure 4. SEM images of FP-a and FP-b ; (a): FP-a(3h), (b):FP-a(6h), (c):FP-a(10h), (d):FP-b(3h), (e):FP-b(6h), (f):FP-b(10h)

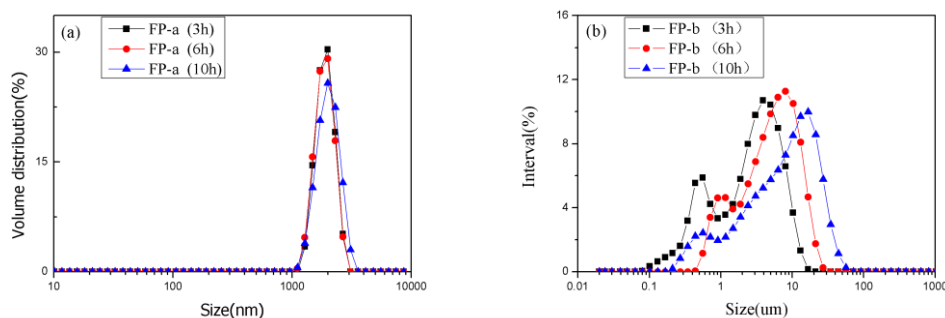


Figure 5. Particle size distributions of FP-a (a) and FP-b (b) at different reaction times

3.3 Synthesis of LiFePO_4/C and its electrochemical performance

The above research results show that there are significant differences in the composition, structure, morphology, particle size, and particle size distribution of iron phosphate samples prepared by the liquid phase precipitation-spray drying method and the hydrothermal method, this will be expected to have different effects on the electrochemical performance of the materials synthesized from them. Therefore, LFP/C-a and LFP/C-b materials are synthesized according to the experimental method described in 2.2.3 of this article used FP-a (10h) and FP-b (10h) samples as raw materials. We study the effects of using different iron phosphates as raw materials on the structure, morphology and properties of synthetic lithium iron phosphate materials.

Figure 6 shows XRD spectrums of LFP/C-a and LFP/C-b materials. It can be seen that the LFP/C-a and LFP/C-b samples all have sharp characteristic diffraction peaks, indicating that the

crystallinity of the two samples is high. During the synthesis of lithium iron phosphate at high temperatures, both amorphous and crystalline iron phosphates have obtained crystalline lithium iron phosphate. This is consistent with the findings of Hany M. Abd EI-Lateef [36]. It is also observed that the XRD spectrums of the two samples are similar to the standard spectrum of lithium iron phosphate (JCPDS card 01-081-1173), indicating that both samples are lithium iron phosphates with an olivine structure which belongs to the orthorhombic system, and the space group is Pnma. No diffraction peak of C is observed in the XRD spectrums of the samples, indicating that carbon is incorporated into the samples in an amorphous form, and a small amount of C has no effect on the structure of the products [22]. The attached table in Figure 6 shows the elemental composition of the LFP/C-a and LFP/C-b samples. It can be seen that the elemental content of the two samples is basically consistent with the theoretical value, and no N element is detected, which indicates that the products have high purity. The N contained in the samples are decomposed and escaped under the action of high temperature without affecting the purity of the lithium iron phosphate, it is consistent with the research results of Dong [38] and Wu [39].

XPS analysis was performed on the materials, and the results are shown in Figure 7a and 7b. Figure 7a is the total spectrums of the elements of the LFP/C-a and LFP/C-b samples. The results show that the spectrums of the samples are completely consistent, and the element composition is Li, Fe, P, O, and C. The corresponding energy spectral peaks are at 54.69, 712.65, 133.84, 531.7 and 284.8 eV, respectively [42]. The XPS results are consistent with the results determined in the attached table of Figure 6, which further shows that the N in the precursor FP-b completely escaped during the synthesis of lithium iron phosphate at high temperature without affecting the structure of the synthesized lithium iron phosphate. Figure 7b shows the peak separation of Fe element using the advantage software. The results show that the Fe elements of the two samples are all Fe^{2+} peaks, indicating that all the Fe^{3+} has been reduced to Fe^{2+} in the atmosphere formed by the added glucose [23, 43].

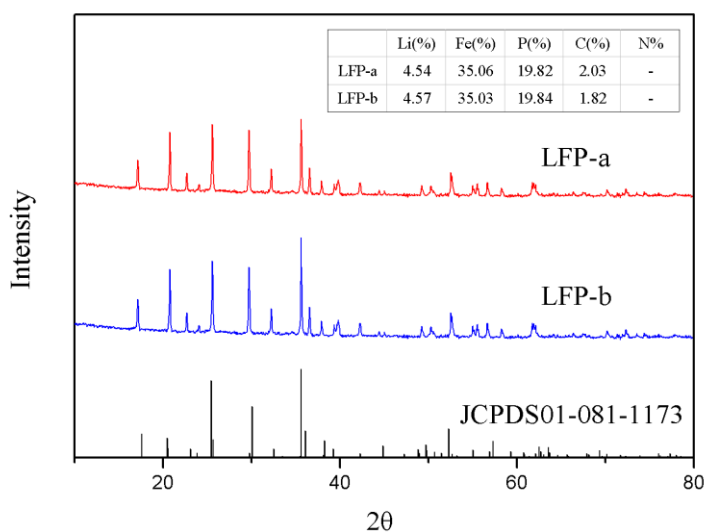


Figure 6. XRD spectrums of LFP/C-a and LFP/C-b samples (The attached table is its element content)

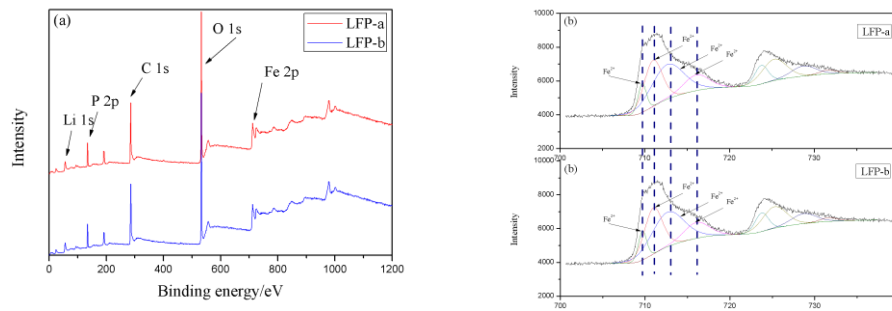


Figure 7. XPS spectrums of LFP/C-a and LFP/C-b samples (a is the total spectrum of elements, b is the spectrum of Fe)

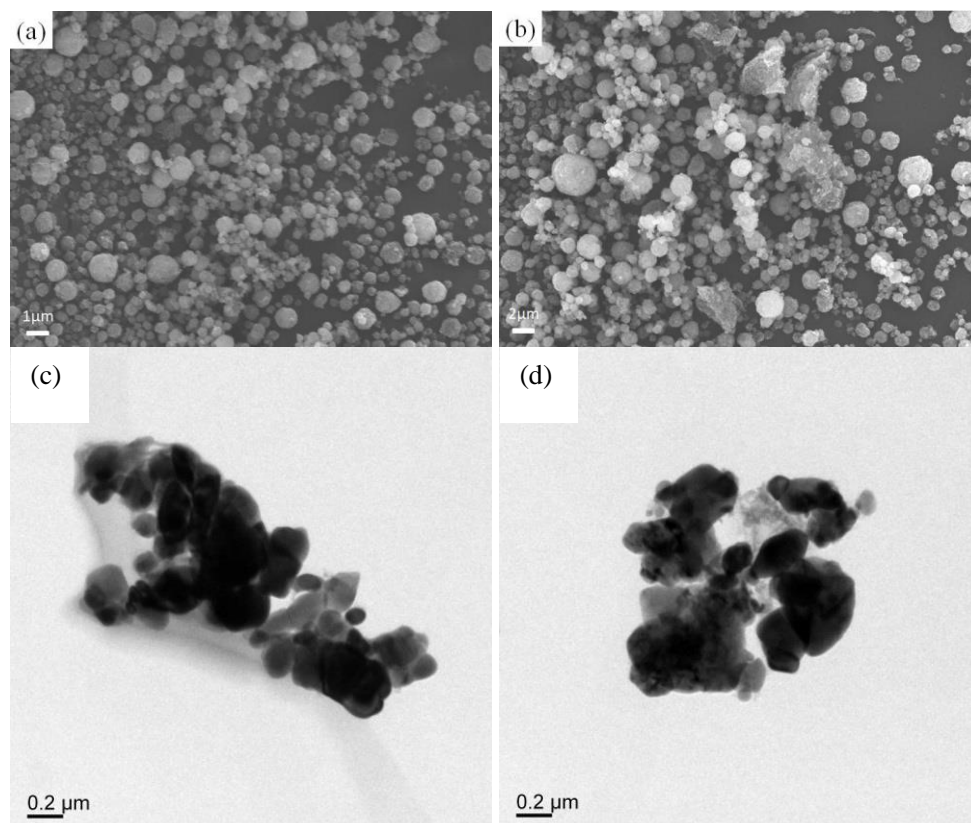


Figure 8. SEM and TEM images of LFP/C-a and LFP/C-b samples

Fig. 8 shows SEM and TEM images of LFP/C-a and LFP/C-b samples, of which Fig. 8a and 8c are SEM and TEM pictures of LFP / C-a, and Fig. 8b and 8d are SEM and TEM images of LFP/C-b. From the SEM images, it can be seen that the spherical morphology of the precursor is well preserved after the LFP/C-a and LFP/C-b materials are synthesized, however, there is also a certain degree of sintering. The sintering phenomenon of LFP/C-a sample is better than that of LFP/C-b sample. This is

because of the spherical FP-b (10h) prepared by the hydrothermal method has poor dispersibility, resulting in a slight agglomeration phenomenon. Sintering occurred during the synthesis of lithium iron phosphate materials. This inference can also be seen from the TEM images of the samples. The TEM images also show that the LFP/C-a and LFP/C-b samples coated a certain amount of carbon, which was consistent with the XPS (Figure 7) spectrums results of the samples.

Figure 9a shows the isothermal adsorption curves of the FP-a (10h) and FP-b (10h) samples, the attached table shows the corresponding specific surface area values. Figure 9b shows the isothermal adsorption curves of LFP/C-a and LFP/C-b materials synthesized with FP-a (10h) and FP-b (10h) as precursors, respectively, and the attached table shows their corresponding specific surface area values. It can be seen from the figures that the isothermal adsorption curves of the precursors FP-a (10h), FP-b (10h) and the synthesized LFP/C-a, LFP/C-b materials all have obvious hysteresis loops. According to the curve fitting results, the specific surface areas of the FP-a(10h) and FP-b(10h) precursors are 50.8739, 28.3905 m^2/g , and the specific surface areas of the LFP/C-a, LFP/C-b materials are 70.1209, 49.1156 m^2/g , respectively. This shows that lithium iron phosphate synthesized by using a high specific surface area iron phosphate precursor also has a higher specific surface area, which will help increase the area of contact between the material and the electrolyte and improve the electrochemical reaction activity [25].

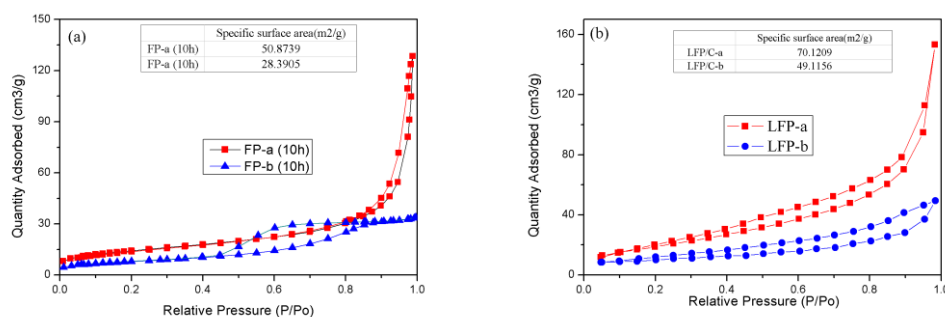


Figure 9. Isothermal adsorption curves of the samples (the attached table is specific surface area)

Figure 10a shows the first charge and discharge performance curves of LFP/C-a and LFP/C-b materials at 0.5 and 10C, respectively. It can be seen that LFP/C-a and LFP/C-b materials have stable charge and discharge platforms at 0.5 and 10C rate conditions. The charge and discharge voltage is about 3.4V, and the discharge voltage at high rate (10C) is slightly falling, however it is still above 3V. Regardless of the low rate (0.5C) or high rate (10C), the difference between the charge and discharge voltage is small, 0.19 and 0.22V, respectively, this is beneficial to improve the reversible performance and stability of the material [22]. The first specific discharge capacities of LFP/C-a and LFP/C-b materials at 0.5 and 10C rates are 155.6, 103.8 mAh/g and 150.4, 95.2 mAh/g , respectively, this shows that LFP/C-a has better first-time charge and discharge performance than that of LFP/C-b at both 0.5 and 10C rates.

Figure 10b shows LFP/C-a and LFP/C-b materials at 0.5, 1, 5 and 10C rate performance curves. It can be seen that the discharge specific capacities of LFP/C-a and LFP/C-b are 150.38 and 150.07 mAh/g, which are almost the same as the initial values when they start to discharge at 0.5C after 1, 5, and 10C rate conditions return to 0.5C again, this shows that the impact of large currents has almost no effect on the electrochemical performance of LFP/C-a and LFP/C-b materials, the discharge specific capacity is almost completely recovered, and the irreversible specific capacity is only 0.22 and 0.33 mAh/g. The first specific discharge capacities of LFP/C-a at 0.5, 1, 5, and 10C rates are 155.6, 149, 119, and 103.8 mAh/g, respectively, while the first specific discharge capacities of LFP/C-b at 0.5, 1, 5, and 10C rates are 150.4, 143.1, 113.7, and 95.2 mAh/g, respectively, which indicate that the discharge specific capacity of LFP/C-a is better than that of LFP/C-b under the above-mentioned conditions, and the LFP/C-a material shows more excellent rate performance. The spherical morphology provides the samples with a high specific surface area, enhances the electrochemical reaction activity, and the small particle size reduces the ion-electron transmission path [44-45], thereby improving the first charge and discharge performance and rate performance. This can be further proved by the cyclic voltammetry curve (Figure 10c) and the AC impedance spectrum (Figure 10d) of the materials.

Figure 10c is the first cyclic voltammetry curves of LFP/C-a and LFP/C-b materials at a scanning speed of 0.1mVs^{-1} . It can be seen that LFP/C-a has a pair of highly symmetrical redox peaks at 3.576 and 3.297 V, while the redox peaks of LFP/C-b are at 3.515 and 3.214 V, respectively. The redox peak corresponds to the desorption and intercalation process of Li^+ [23], indicating that a redox reaction between lithium iron phosphate and iron phosphate has taken place. It can be seen that the potential differences of the redox peaks of LFP/C-a and LFP/C-b are 0.279 and 0.301 V, respectively, the potential difference can determine the reversibility of the redox reaction [46], LFP/C-a has a smaller potential difference and exhibits better electrochemical performance.

Figure 10d is the AC impedance curves of LFP/C-a and LFP/C-b materials and the attached drawing is corresponding equivalent circuit. As can be seen from the figure, the AC impedance curves of the two samples are composed of a compression semicircle in the high frequency region and a diagonal line in the low frequency region, the semicircle in the high frequency region corresponds to the charge transfer process in the electrochemical reaction, and the diagonal line in the low frequency region corresponds to the diffusion process of Li^+ in the bulk phase of the material [47]. According to the results of the equivalent circuit diagram fitting, it can be known that the Rct values of LFP/C-a and LFP/C-b materials are 42.09 and 54.25 Ω , respectively, which indicates that LFP/C-a has a lower charge transfer impedance. This is conducive to reducing the capacity attenuation during the cyclic charging and discharging of the material, and improving the cyclic stability performance of the samples. This is consistent with the results of the cyclic voltammetry curve shown in Fig 10c.

Therefore, the material prepared in this work exhibits excellent electrochemical performance from the above experimental results. We lists the performance of similar cathode materials reported in other literatures showed in table 1, from which we can see it has better performance than other materials.

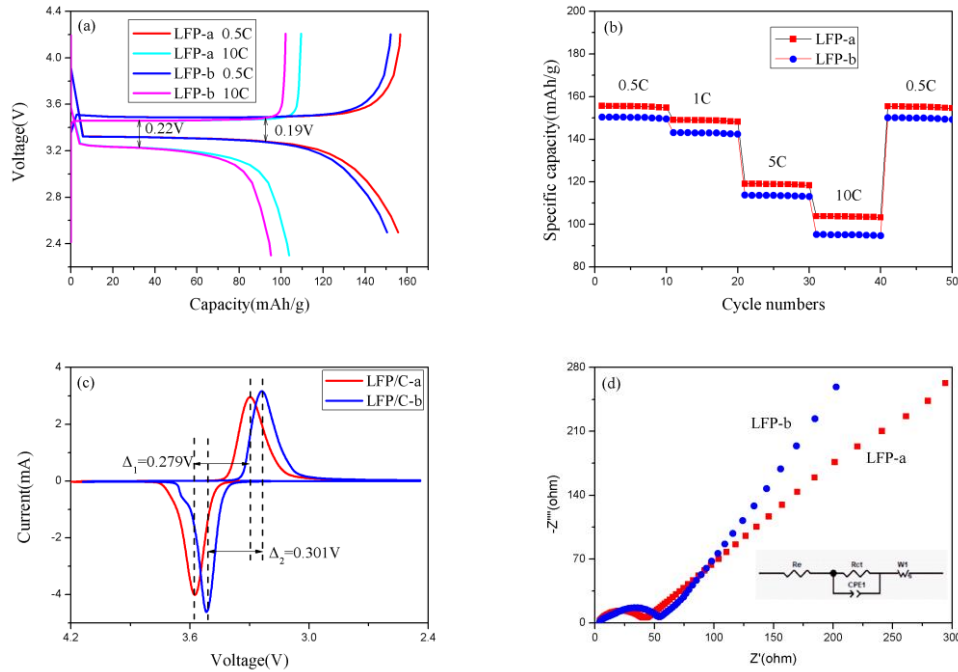


Figure 10. LFP/C-a, LFP/C-b electrochemical performance (a is the first charge and discharge curves; b is the rate performance curves; c is the cyclic voltammety curves, and d is the AC impedance spectrums)

Table 1. Comparison between electrochemical performance of the LiFePO_4/C with those in the literature

Method	morphology	Initial discharge capacity (mAh/g)	Ref
Liquid precipitation	Porous	162.43 (0.5c) 154.35 (1c)	21
Hydrothermal	Rice grain	148.13 (1c)	22
Hydrothermal	Random particles	136.4 (0.1c) 109.9 (1c)	23
Hydrothermal	Spherical	176 (0.1c)	25
Hydrothermal	Cubic	156 (0.1c)	25
Hydrothermal	Multi-armed	142 (0.1c)	25
Hydrothermal	Cross-like	135 (0.1c)	25
Liquid precipitation	Spherical	159.29 (0.1c) 151.78 (0.2c) 112.11 (5c) 155.6 (0.5c)	27
Liquid Precipitation-Spray Drying	Spherical	149 (1c) 119.1 (5c)	This work

4. CONCLUSIONS

Spherical iron phosphate was prepared by liquid phase precipitation-spray drying method and hydrothermal method, respectively. Compared with the hydrothermal method, the samples prepared by liquid phase precipitation-spray drying method has better spherical consistency, finer particles, more uniform particle size distribution, and larger specific surface area. These excellent properties are retained in the synthesis of lithium iron phosphate / carbon composite materials, which enabled the synthetic material to have a higher charge-discharge specific capacity, better rate and cycle performance, and lower charge transfer resistance. Compared with the hydrothermal method, the liquid-phase precipitation-spray drying method also has the advantages of simple process and easy operation. Therefore, the liquid phase precipitation-spray drying method is expected to have a very good prospects for practical application.

CONFLICTS OF INTEREST

There are no conflicts to declare.

References

1. P.Z. Zhao, H.B. Liu and H.H. Zheng, *Mater. Lett.*, 123 (2014) 128.
2. L. Liu and X.L. Chen, *Iran. Polym. J.*, 24 (2015) 337.
3. X. Wang, J. Zhuang and Q. Peng, *Nat. Chem.*, 437 (2005) 121.
4. Z.T. Deng, L. Cao, F.Q. Tang and B.S. Zhou, *J. Phys. Chem. B*, 109 (2005) 16671.
5. M. Pramanik, Y. Tsujimoto, V.X. Malgras, S.X. Dou, J. Ho and K.Y. Yamauchi, *J. Mater. Chem. B*, 27 (2015)1082.
6. M. Pramanik, M. Imura, J.J. Lin, J.H. Kim and Y. Yamauchi, *Chem. Commun.*, 51 (2015)13806.
7. L. Wang, C.V. Putnis, E.R. Agudo, J. Hövelmann and A. Putnis, *Sci. Technol.*, 49 (2015)4184.
8. Y. Zhang, Z.F. Yi, J.S. Wang, L.M. Wei, L.X. Kong and L.J. Wang, *Mater. Lett.*, 233 (2018)290.
9. R. Lin and Y. Ding, *Mater.*, 6 (2013)217.
10. Y.Y. Liu, H. Liu, L.W. An, X.X. Zhao and G.C. Liang, *Ionics*, 25 (2019)61.
11. C.V. Ramana, A. Mauger and F. Gendron, *J. Power Sources*, 187 (2009)555.
12. P. Ajibade and N. Zulu, *J. Coord. Chem.*, 63 (2010)11.
13. W. Xiang, E.H. Wang, M.Z. Chen, H.H. Shen, S.L. Chou, H. Chen, X.D. Guo, B.H. Zhong and X.L. Wang, *Electrochim. Acta*, 178 (2015)353.
14. D. Sana, T. Beno and H. Amer, *Energy Storage*, 18 (2018)259.
15. S. Khateeb and T. Sparks, *J. Mater. Sci.*, 54 (2019)4089.
16. X.Y. Wu, Z.G. Zou, S.Y. Li and Q. Yang, *J. Electroanal. Chem.*, 829 (2018)20.
17. S. Guo, G.K. Zhang and J.C. Yu, *J. Colloid Interface Sci.*, 448 (2015)460.
18. K.P. Singh, E.J. Bae and J.S. Yu, *J. AM. CHEM. SOC.*, 137 (2015)3165.
19. R.H. Lin, A.P. Amrute, F. Krumeich, K. Lázár, R. Hauert, M. Yulikove and J.P. Ramírez, *CrystEngComm.*, 18 (2016)3174.
20. X. Yang, J.X. Zhang and S.M. Zhang, *Mater. Res. Express*, 6 (2012)347.
21. X.M. Guan, G.J. Li, C.Y. Li and R.M. Ren, *T. Nonferr. Metal. Soc.*, 27 (2017) 141.
22. Y. Li, J. Wang, J. Yao, H.X. Huang, Z.Q. Du, H. Gu and Z.T. Wang, *Mater. Chem. Phys.*, 224 (2019) 293.
23. J. Xia, F.L. Zhu, G.R. Wang, L. Wang, Y.S. Meng and Y. Zhang, *Solid State Ionics*, 308 (2017) 133.
24. H. Liu, C. Li, H.P. Zhang, L.J. Fu, Y.P. Wu and H.Q. Wu, *J. Power Sources*, 159 (2006) 717.
25. S.M. Zhang, J.X. Zhang, S.J. Xu, X.J. Yuan and T. Tan, *J. Power Sources*, 243 (2015) 274.

26. T.T. Zhan, W.F. Jiang, C. Li, X.D. Luo, G. Lin, Y.W. Li and S.H. Xiao, *Electrochim. Acta*, 246(2017) 322.
27. X. Ke, R.G. Xiao, X. Liao, Z.M. Ma, S.D. Wang and D. Xu, *J. Electroanal. Chem.*, 820 (2018) 18.
28. Y.M. Zhu, S.Z. Tang, H.H. Shi and H.L. Hu, *Ceram. Int.*, 40 (2014) 2685.
29. G. Lin, W.F. Jiang, M. Yuan, W. Zeng, Y.W. Li, J.W. Yang and S.H. Xiao, *J. Alloys Compd.*, 782 (2019) 176.
30. Y. Liu, S.J. Xu, S.M. Zhang, J.X. Zhang, J.C. Fan and Y.R. Zhou, *J. Mater. Chem.*, 30 (2015) 5501.
31. Y. Liu, Y.R. Zhou, J.X. Zhang, S.M. Zhang and P. Ren, *J. Power Sources*, 314 (2016) 1.
32. T.B. Zhang, X.B. Cheng, Q. Zhang, Y.C. Lu and G.S. Luo, *J. Power Sources*, 324 (2016) 52.
33. F. Fathollahi, M. Javanbakht, H. Omidvar and M. Ghaemi, *J. Alloys Compd.*, 627 (2015) 146.
34. X.W. Liu, T.Z. Feng, S.H. Chen and H. Wei, *Int. J. Electrochem. Sci.*, 11 (2016) 227.
35. R.Q. Ding, H. Liu, L. Wang and G.C. Liang, *Ionics*, 25(2019) 5633.
36. H.M. Lateef, A.H. Touny and M.M. Saleh, *Mater. Res. Express*, 5 (2018)1.
37. H.J. Song, Y.L. Sun and X.H. Jia, *Mater. Charact.*, 107 (2015) 182.
38. B. Dong, G. Li, X.G. Yang, L.M. Chen and G.Z. Chen, *Ultrason. Sonochem*, 42 (2018) 452.
39. K.P. Wu, D.W. Liu and Y. Tang, *Ultrason. Sonochem*, 40(2018) 832.
40. K. VEDIAPPAN, A. GUERFI, V. GARIÉPY, G.P. DEMOPOULOS, P. HOVINGTON, J. TROTTIER, A. MAUGER, C.M. JULIEN and K. ZAGHIB, *J. Power Sources*, 266 (2014) 99.
41. F. Yang, H. Zhang, Y.J. Shao, H.Y. Song, S.J. Liao and J.W. Ren, *Ceram. Int.*, 43 (2017) 16652.
42. L.Y. Zhang, Y.F. Tang, Z.Q. Liu, H.N. Huang, Y.Z. Fang and F.Q. Huang, *J. Alloys Compd.*, 627 (2015)132.
43. Y.Q. Chen, K.X. Xiang, W. Zhou, Y.R. Zhu, N.B. Bai and H. Chen, *J. Alloys Compd.*, 749 (2018) 1063.
44. C.C. Yang, J.H. Jang and J.R. Jiang, *Energy Procedia.*, 61 (2014) 1402.
45. X.Y. Zeng, Q.B. Liu, M.F. Chen, L.M. Leng, T. Shu, L. Du, H.Y. Song and S.J. Liao, *Electrochim. Acta*, 177 (2015) 277.
46. K. VEDIAPPAN, A. GUERFI, V. GARIÉPY, G.P. DEMOPOULOS, P. HOVINGTON, J. TROTTIER, A. MAUGER, C.M. JULIEN and K. ZAGHIBA, *J. Power Sources*, 266 (2014) 99.
47. C. Gao, J. Zhou, G.Z. Liu and LinWang, *J. Alloys Compd.*, 727(2017)501.
48. H.W. Liu, H.M. Yang and J.L. Li, *Electrochim. Acta*, 55(2010) 1626.